Computers in Biology and Medicine 42 (2012) 523–537

Contents lists available at SciVerse ScienceDirect

Computers in Biology and Medicine

journal homepage: www.elsevier.com/locate/cbm

Segmentation of interest region in medical volume images using geometric deformable model ☆

Myungeun Lee [a,*], Wanhyun Cho [1,b], Sunworl Kim [2,b], Soonyoung Park [3,c], Jong Hyo Kim [4,d]

[a] Medical Research Center, Seoul National University, #303 Biomedical Research Institute 1, 101 Daehak-ro, Jongno-gu, Seoul 110-744, South Korea
[b] Department of Statistics, 300 Yongbong-dong, Buk-gu, Gwangju 500-757, South Korea
[c] Department of Electronics Engineering, Mokpo National University, 61 Dorim-ri, Chungkye-myun, Muan-gun, Jeonnam 534-729, South Korea
[d] Department of Intelligent Convergence Systems, Graduate School of Convergence Science and Department of Radiology, College of Medicine, Seoul National University, 101 Daehak-ro, Jongno-gu, Seoul 110-744, South Korea

ARTICLE INFO

Article history:
Received 21 January 2011
Accepted 12 January 2012

Keywords:
Medical volume images segmentation
Geometric deformable model
Calculus of variation principle
Level set method
Hybrid speed function

ABSTRACT

In this paper, we present a new segmentation method using the level set framework for medical volume images. The method was implemented using the surface evolution principle based on the geometric deformable model and the level set theory. And, the speed function in the level set approach consists of a hybrid combination of three integral measures derived from the calculus of variation principle. The terms are defined as robust alignment, active region, and smoothing. These terms can help to obtain the precise surface of the target object and prevent the boundary leakage problem. The proposed method has been tested on synthetic and various medical volume images with normal tissue and tumor regions in order to evaluate its performance on visual and quantitative data. The quantitative validation of the proposed segmentation is shown with higher Jaccard's measure score (72.52%–94.17%) and lower Hausdorff distance (1.2654 mm–3.1527 mm) than the other methods such as mean speed (67.67%–93.36% and 1.3361 mm–3.4463 mm), mean-variance speed (63.44%–94.72% and 1.3361 mm–3.4616 mm), and edge-based speed (0.76%–42.44% and 3.8010 mm–6.5389 mm). The experimental results confirm that the effectiveness and performance of our method is excellent compared with traditional approaches.

1. Introduction

Segmentation is the process of separating objects in an image. For volume medical images, its field of application is wide. For example, 3D visualizations of anatomic structures could benefit enormously from exact segmentation. Thus, volume segmentation is becoming an increasingly important part of computer-based medical applications for diagnosis and analysis of anatomical data. However, segmentation in medical imaging is considered to be a very difficult problem, even though methods specialized for a particular volume usually provides better results [1]. Recently, the use of a geometric deformable model approach to extract the deformable surface from a volume image has become very common [2]. In particular, many researchers have explored the use of deformable models for volume segmentation. Active deformable models are the most popular methods for the volume segmentation of Region-Of-Interest (ROI) in medical images, implicitly in the form of a level set function or explicitly as a snake function. Moreover, the popularly of the level set method has increased because it can handle complex geometries and topological changes. The level set is a shape-driven tool based on a defined speed function that can grow and shrink and take the shape of any complex object of interest. The level set method does not generally depend on the parameters settings of the model [3]. This makes it a very attractive and flexible method for shape modeling and object detection. Another advantage of the level set approach is that the entire segmentation procedure is fully automatic and is based on the initial model. Unlike other methods, the extension of the algorithm to a volume dataset is straightforward and does not require additional mechanisms. These properties make the level set method a state-of-the-art method for segmentation, especially volume segmentation. Therefore, the focus of our paper is on a geometric deformable model for ROI segmentation in medical images.

☆ Grants:
This research was supported by Basic Science Research Program through the National Research Foundation of Korea (NRF) funded by the Ministry of Education, Science and Technology (2011-0004970).
This research was supported by Basic Science Research Program through the National Research Foundation of Korea (NRF) funded by the Ministry of Education, Science and Technology (2011-0014828).
The research was supported by the Converging Research Center Program through the Ministry of Education, Science and Technology (2011K000718).

* Corresponding author. Tel.: +82 2 2072 1760; fax: +82 2 747 1762.
E-mail addresses: melee@snu.ac.kr (M. Lee), whcho@jnu.ac.kr (W. Cho), sunworl@gmail.com (S. Kim), sypark@mokpo.ac.kr (S. Park), kimjhyo@snu.ac.kr (J.H. Kim).
[1] Tel.: +82 62 530 3443.
[2] Tel.: +82 62 530 0443.
[3] Tel.: +82 61 450 2434.
[4] Tel.: +82 2 2072 3677; fax: +82 2 747 1762.

0010-4825/$ - see front matter © 2012 Elsevier Ltd. All rights reserved.
doi:10.1016/j.compbiomed.2012.01.005

However, it is difficult to detect object volumes based on an active contour model that is sensitive to certain circumstances. One problem is that the active contour formulation entails the tuning of several parameters. In order to overcome the difficulty of adjusting parameters, a partial differential equation is used for immediate user feedback on the parameter settings of the active contour model. The user can tune the parameters and control the shape of the active contour model by solving the partial differential equation [4,5]. In particular, Leventon et al. performed more generic and automated detection of tumor regions through level set evolution with statistical shape information [6]. But, the disadvantage of their method is that it may be difficult to obtain statistical prior knowledge in various cases, especially for tumor segmentation. T. Chan et al. proposed active contours to detect object regions in a given image based on the theory of curve evolution and level sets without boundary information [7]. Also, level set approaches based on K-mean clustering and fuzzy classification are proposed in [8–10]. In these methods a clustering step is performed and the deformable model then grows on top of the clustered pixels. For the speed function of the level set, Ho et al. implemented the histogram of a difference image fitted by parametric distributions for both the enhanced parts and the noisy background [11]. Many level set algorithms may be distinguished on the basis of their speed functions. Some approaches, for example, require user interaction while others rely on prior estimation of the tumor density function [12].

In this paper, we are interested in segmentation of tumor and normal tissue in medical volume images using geometric deformable models based on evolution theory and the level set method. Our approach handles topological changes of deformable surfaces using several geometric integral measures. These measures are derived by the hybrid method, which considers a region and boundary information for tumor tissue. They contain three terms called robust alignment, active region, and smoothing. First, the alignment term should move the model towards the boundaries of objects given in the input images dataset. This is decided by the inner product of the surface normal and the gradient of an input image for which the normal best aligns with the image gradient. Second, the active region term efficiently splits the interior and exterior of the surface of the object. This model can not only overcome some of the weaknesses in the boundary-based model such as dependency of local information and initialization, but it can also optimally partition a given image into some homogenous regions. Third, the smoothing term helps to ensure a smooth surface by eliminating noise. This is determined by the mean curvature computed at a given point. The new method is iteratively applied with the weighted average of three terms until we obtain the optimal segmentation result. Finally, we have proposed an algorithm that can update the parameter values iteratively. This also provides the basis for a numerical scheme that is used by geometric deformable models.

The remainder of our paper consists of five sections. In Section 2, we introduce the active deformable model and the level set theory. Section 3 proposes the hybrid speed function in the level set method. Section 4 provides a detailed analysis of the accuracy and robustness of the proposed algorithm. In Section 5, we show the various segmentation results for medical volume images, and we conclude our paper in Section 6.

2. Active deformable model

2.1. Geometric integral measures for active surfaces

Let $S(r,s):\Re^2\rightarrow\Re^3$ be a parameterized two-dimensional surface in 3D space defined as follows: $S(r,s)=\{(x(r,s),y(r,s),z(r,s)): 0\le r\le L_1, 0\le s\le L_2\}$. Then, the energy functional $E(S)$ for a surface S can be defined as two types of integral measures that are related via the Green theorem [13]. The first functional integrates the function $g(S(r,s))$ defined on the surface, and is considered as a surface based measure in the general form of:

$$E_1(S)=\int_0^{L_1}\int_0^{L_2} g(S(r,s))drds. \tag{1}$$

The second functional integrates the values of the function $f(x,y,z)$ inside the surface, and is usually referred to as a volume based measure,

$$E_2(S)=\iiint_{\Omega_S} f(x,y,z)dxdydz. \tag{2}$$

Formally, we search for the optimal surface S, such that

$$S=\underset{S}{\operatorname{argmin}}E(S) \text{ or } S=\underset{S}{\operatorname{argmax}}E(S). \tag{3}$$

In this case, if we have a surface integral of the general form:

$$E(S)=\iint_S L(S(r,s))drds, \tag{4}$$

then the surface that minimizes (or maximizes) this functional, can be identified by a partial differential equation known as the Euler–Lagrange equation:

$$\frac{\partial E(S)}{\partial S}=\begin{cases}\frac{\partial L}{\partial x}-\frac{\partial}{\partial r}\frac{\partial L}{\partial x_r}-\frac{\partial}{\partial s}\frac{\partial L}{\partial x_s}=0\\ \frac{\partial L}{\partial y}-\frac{\partial}{\partial r}\frac{\partial L}{\partial y_r}-\frac{\partial}{\partial s}\frac{\partial L}{\partial y_s}=0\\ \frac{\partial L}{\partial z}-\frac{\partial}{\partial r}\frac{\partial L}{\partial z_r}-\frac{\partial}{\partial s}\frac{\partial L}{\partial z_s}=0\end{cases}. \tag{5}$$

A dynamic process known as gradient descent that moves an arbitrary surface towards a minimum (or maximum) of $E(S)$, is given by the surface evolution equation:

$$\frac{\partial S}{\partial t}=-\frac{\partial E(S)}{\partial S}, \tag{6}$$

where we added a virtual time parameter t to our surface in order to allow its evolution into a family of surfaces $S((r,s),t)$. The key idea is to evolve the surface S from some initialization, in the direction of the negative energy gradient, and this is implemented by the gradient descent equation:

$$\frac{\partial S}{\partial t}=-\frac{\partial E(S)}{\partial S}=F\cdot\vec{N}. \tag{7}$$

It models evolution along the normal $\vec{N}$ with a speed function F.

2.2. Representing an active surface with the level set approach

When considering an active surface model for segmenting 3D volume data, one option is to adopt an implicit representation of a surface using the level set model. This method specifies a surface S as a level set of a 3D scalar volume function:

$$\phi:\Omega\times\Re^+\rightarrow\Re, \tag{8}$$

where $\Omega\subset\Re^3$ is the range of the surface model. Thus, a surface S can be expressed as the following level set:

$$S=\{w|\,\phi(w,t)=k\}. \tag{9}$$

For a surface which evolves along the normal $\vec{N}$ with a speed F, one can derive a corresponding partial differential equation for the embedding function ϕ in the following manner [3]. Since the function ϕ always takes a zero value on the surface, the total time derivative of ϕ at the surface locations must vanish:

$$\nabla\phi(w,t)\frac{\partial S}{\partial t}+\frac{\partial\phi(w,t)}{\partial t}=0 \tag{10}$$

By inserting the definition of the normal $\vec{N} = -(\nabla\phi/|\nabla\phi|)$, we can obtain the evolution equation for ϕ:

$$\phi_t = \frac{\partial\phi}{\partial t} = |\nabla\phi| \cdot F. \tag{11}$$

By derivation, this equation only specifies the evolution of ϕ and the values of the speed function F at the location of the surface.

Because the evolution of the surface is equivalent to the evolution of the level set function, a surface can be defined as the border between the positive and negative areas of the level set function. So the surface can be identified simply by checking the sign of the level set function ϕ. Furthermore, the initial level set function ϕ_0 can be based on the signed distance from the initial surface as given by:

$$\phi_0(w) = \pm D(w, N_w(S_0)), \tag{12}$$

where $\pm D(a,b)$ denotes the signed distance between a and b, and $N_w(S_0)$ denotes the nearest neighboring voxel on initial surface S_0. And the initial level set function ϕ_0 is zero at the initial surface points of S_0.

2.3. Boundary and region information models for active surfaces

In general, active surface models can be broadly classified into two basic deformable models. They are the boundary-based models (which are often referred to as edge-based) that rely on the generation of a strength image and the extraction of prominent edges, and region-based models that rely on the homogeneity of spatially localized features and properties.

The models based on boundary information have used local filtering techniques such as edge detection operators. These models can provide a closed curve as a compromise between the regularity of the curve and important boundary features. Recently, Caselles et al. [16] have proposed the geodesic active contour model in combination with the level set theory. This is one method of exploring the geometric interpretation of geodesic active contours from the point-of-view of object segmentation as well as its relation to other geometric curve evolution approaches to active contours. This model can be expressed as the following formula:

$$\frac{\partial C}{\partial t} = g(I)\kappa\vec{N} - (\nabla g \cdot \vec{N})\vec{N} \tag{13}$$

where κ is the Euclidean curvature and $\vec{N}$ is the unit inward normal vector.

The region-based models are more suitable for dealing with frame partition problems. Chan and Vese [7] have proposed an active contour model that minimizes the fitting energy function. In this case, the fitting energy is defined by:

$$F_1(C) + F_2(C) = \frac{1}{2}\int_{inside(C)} |u_0(x,y) - c_1|^2 dxdy + \frac{1}{2}\int_{outside(C)} |u_0(x,y) - c_2|^2 dx\,dy \tag{14}$$

where C is the evolving curve, and the constants c_1 and c_2, depending on C, are the averages of image intensity u_0 inside C and outside C, respectively.

Recently, Wang et al. [27] presented and discussed the details of an efficient local Chan–Vese (LCV) model and its numerical implementation. The overall energy functional in the proposed LCV model E^{LCV} consists of three parts: global term E^G, local term E^L and regularization term E^R. Thus the overall energy functional can be described as:

$$E^{LCV} = \alpha \cdot E^G + \beta \cdot E^L + E^R. \tag{15}$$

The global term E^G is directly derived in the Chan–Vese model in which it is also called the fitting term. It can be seen that the global term is defined based on the global properties, i.e., the averages of μ_0 inside C and outside C, which is stated as equation (14).

The local term is used for local statistical information as the key to improve the segmentation capability of the [27] model on images with intensity in-homogeneity.

$$E^L(d_1,d_2,C) = \int_{inside(C)} |g_k \cdot u_0(x,y) - u_0(x,y) - d_1|^2 dxdy + \int_{outside(C)} |g_k \cdot u_0(x,y) - u_0(x,y) - d_2|^2 dxdy \tag{16}$$

where g_k is an averaging convolution operator with a $k \times k$ size window, and d_1 and d_2 are the intensity averages of difference image $g_k \cdot u_0(x,y) - u_0(x,y)$ inside C and outside C, respectively.

Finally, in order to control the smoothness of the zero level set and further avoid the occurrence of small, isolated regions in the final segmentation, they add a regularization term or a length penalty term $L(C)$, which is defined to be related to the length of the evolving curve C. The length functional can be written as:

$$L(C) = \oint_C dp. \tag{17}$$

In this case, through replacing the curve C by the level set function $\phi(x,y)$, $L(C)$ can be reformulated as:

$$L(\phi = 0) = \int_\Omega |\nabla H(\phi(x,y))| dxdy = \int_\Omega \delta(\phi(x,y)) |\nabla\phi(x,y)| dxdy, \tag{18}$$

where $H(z)$ and $\delta(z)$ is the Heaviside and Dirac delta function, respectively.

Hence, our approach handles topological changes of deformable surfaces using several geometric integral measures. These measures will be derived by a hybrid method, which combines surface information, volume information and regularities of 3D tissues in medical volume images.

3. Hybrid speed function based on integral measure

3.1. Robust alignment term

First, we are aiming to propagate an initial surface S that approximates as closely as possible an object's surface given medical volume images. To this end, we use a geometric functional that is expressed by the inner product between the volume image gradient and the surface normal. It is reasonable to assume that in many cases the gradient direction is a good estimator of the orientation of the evolving surface. The inner product will be a high value if the surface normal aligns with the gradient direction of the volume images.

But, in case of images with intensity in-homogeneity, the gradient term can never fully stop the level set evolution even for idea edges, which often makes leakage inevitable. Hence, we explore a new edge indicator vector embedded with a speed term. One type of ideal selection is to choose an edge indicator vector such as the Gradient Vector Flow (GVF) field proposed in Xu et al. [14]. The particular advantages of this field are its insensitivity to initialization and its ability to move into boundary concavities. To obtain the GVF field, we first begin to define the edge map $f(\mathbf{x})$ derived from the image intensity $I(\mathbf{x})$ having the property that it is larger near the volume images edges. Next, we can define the GVF field with a vector field $\mathbf{V}_{GVF}(\mathbf{x})$ that minimizes the energy functional [15]:

$$E(\mathbf{V}_{GVF}) = \int_{\Re^3} (\mu|\nabla\mathbf{V}|^2 + |\nabla f|^2|\mathbf{V} - \nabla f|^2) d\mathbf{x} \tag{19}$$

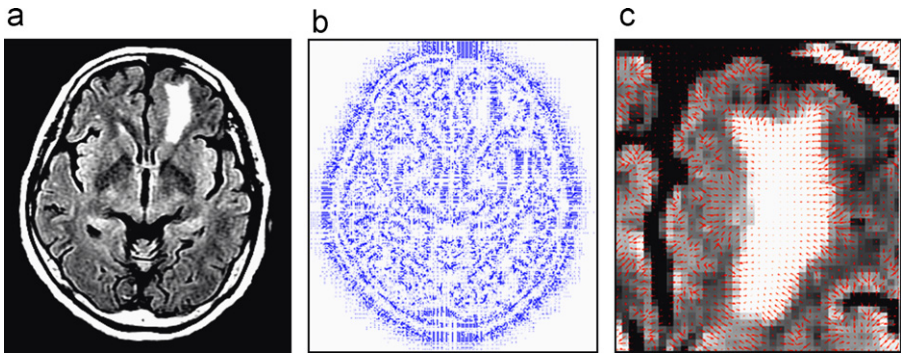

Fig. 1. Computation of the Gradient Vector Flow (GVF) in a patient with a tumor. (a) Brain original MR image, (b) GVF computed from the edge map, and (c) details of the normalized GVF in the brain tumor region.

where the parameter μ is a regularization parameter governing the tradeoff between the first and second term in the integrand. This parameter should be set according to the amount of noise present in the image (for more noise, increase μ). The gradient operator ∇ is applied to each component of $\mathbf{V}_{GVF}$ separately. Using the calculus of variations, we find that the GVF field must satisfy the Euler equation

$$\mu\nabla^2\mathbf{V}-|\nabla f|^2(\mathbf{V}-\nabla f)=0, \tag{20}$$

where ∇^2 is also applied to each component of the vector field $\mathbf{V}_{GVF}$ separately. Fig. 1 shows the computation results of the gradient vector flow for MR head images with a tumor region.

Finally, if we replace the image gradient vector field with the GVF field in the robust alignment measure representing the absolute value of the inner product between the vector field and the surface normal, we obtain the following functional:

$$E_A(S)=\iint_S \langle \mathbf{V}_{GVF},\vec{N}\rangle dsdr. \tag{21}$$

By the variational principle, the extremals of this functional $E_A(S)$ can be identified by the Euler Lagrange equation. It is given by the surface evolution equation:

$$\frac{\partial S}{\partial t}=sign(\langle \mathbf{V}_{GVF},\vec{N}\rangle)div(\mathbf{V}_{GVF})\vec{N}. \tag{22}$$

So, the corresponding surface evolution equation of this level set formulation is given by:

$$\frac{\partial \phi}{\partial t}=sign(\langle \mathbf{V}_{GVF},\nabla\phi\rangle)div(\mathbf{V}_{GVF})|\nabla\phi|. \tag{23}$$

Hence, we can obtain a new speed function, which is utilized as a robust alignment term as follows:

$$F=sign(\langle \mathbf{V}_{GVF},\nabla\phi\rangle)div(\mathbf{V}_{GVF}). \tag{24}$$

3.2. Active region term

Next, let us consider the active surface model that uses the region information of the target objects for segmentation. This model can not only overcome some of the weaknesses in the boundary-based model such as dependency of local information and initialization, but can also optimally partition a given image into some homogenous regions.

First, we assume that a regular surface S splits a volume image domain Ω into two disjoint volumes Ω_1 and Ω_2. We also assume that all partitions are equally probable, that is:

$$p(I|\{\Omega_1,\Omega_2\})=p(I|\Omega_1)p(I|\Omega_2) \tag{25}$$

and the voxels within each volume are independent:

$$p(I|\Omega_i)=\prod_{w\in\Omega_i} p(I(w)),\quad i=1,2. \tag{26}$$

Then the joint probability of intensity values I observed at a given volume partition $\Omega=\{\Omega_1,\Omega_2\}$ is given by:

$$p(I|\{\Omega_1,\Omega_2\})=p(I|\Omega_1)p(I|\Omega_2)=\prod_{w\in\Omega_1} p_1(I(w))\prod_{w\in\Omega_2} p_2(I(w)). \tag{27}$$

In this case, the optimal segmentation is found by minimizing the following energy functional:

$$E(S(\Omega_1,\Omega_2))=-\left(\int_{\Omega_1}(\log p_1(I(w)))dw+\int_{\Omega_2}(\log p_2(I(w)))dw\right). \tag{28}$$

Using the Heaviside function H and the one-dimensional Dirac measure δ concentrated at zero, defined respectively as:

$$H(z)=\begin{cases}1, & \text{if}\quad z\geq 0\\ 0, & \text{if}\quad z<0\end{cases}\quad\text{and}\quad \delta(z)=\frac{d}{dz}H(z), \tag{29}$$

we can express the above energy functional in the following level set form:

$$E(\phi)=-\left(\int_{\Omega}H(\phi(w))\log p_1(I(w))dw+\int_{\Omega}(1-H(\phi(w))\log p_2(I(w))dw\right). \tag{30}$$

Then, the corresponding Euler–Lagrange evolution equation for ϕ is given by:

$$\frac{\partial\phi}{\partial t}=\delta(\phi(w))(\log p_1(I(w))-\log p_2(I(w))). \tag{31}$$

After a standard rescaling that involves replacing $\delta(\phi)$ with $|\nabla\phi|$, we have the following equation:

$$\phi_t=|\nabla\phi(w)|(\log p_1(I(w))-\log p_2(I(w))). \tag{32}$$

In this case, we have assumed that the probability distribution of the intensity value is generally modeled by Gaussian distribution. Moreover, since the volume of an interest object such as a tumor (Ω_1) is homogeneous, it is sufficient to model this as a single Gaussian distribution. However, since the outside of a tumor such as a normal volume (Ω_2) consists of several tissues, it needs to be represented by a Gaussian mixture model with the proper number of components. However, in spite of the complex structures of the outside volume, we have conveniently used a single Gaussian distribution to model its probability distribution. Thus, the respective probability distributions of the pixel values in each volume Ω_i are given by:

$$p_i(I(w))=\varphi(I(w);\mu_i,\sigma_i^2),$$
$$\varphi(I(w);\mu_i,\sigma_i^2)=(2\pi\sigma_i^2)^{-1/2}\exp\left(-\tfrac{1}{2\sigma_i^2}(I-\mu_i)^2\right),\quad i=1,2, \tag{33}$$

where μ_i, σ_i^2, $i=1,2$ are respectively the means and variances of each Gaussian distribution. The parameters $\{\mu_i,\sigma_i^2\}$, $i=1,2$ in the probability distribution of the tumor region can be estimated by applying the Maximum Likelihood

method as follows:

$$\hat{\mu}_i = \frac{1}{|\Omega_i|}\sum_{w\in\Omega_i} I(w), \quad \hat{\sigma}_i^{\,2} = \frac{1}{|\Omega_i|-1}\sum_{w\in\Omega_i}(I(w)-\hat{\mu}_i)^2, \quad i=1,2. \tag{34}$$

3.3. Smoothing term

One of the functionals related to a smoothing measure for a surface is known as the geodesic active surface model. This model was introduced in Caselles et al. [16] as a geometric alternative to the snake's method. The model is derived using a variation principle from a geometric measure, and it is defined by:

$$E_G(S) = \int_0^{L_1}\int_0^{L_2} g(S(r,s))drds. \tag{35}$$

If the function $g(x,y,z)$ is given in a form such as $g(x,y,z)=1/(1+|\nabla I(x,y,z)|^2)$, then it is based on integration of an inverse edge indicator function along the surface. It represents a search for a surface along which the inverse edge indicator results in the smallest possible values. That is, we are aiming to find the surface S that minimizes this functional. The geodesic active surface usually serves as a good regularization term in a noisy image. The Euler–Lagrange equation known as the gradient descent process is given by the following evolution equation:

$$\frac{\partial E_G(S)}{\partial S} = (g(S)\kappa - \langle \nabla g, \vec{N}\rangle)\vec{N}. \tag{36}$$

In this case, κ is the mean curvature of the surface. Then, the corresponding Euler–Lagrange evolution equation for the level set function ϕ is given by:

$$\frac{\partial \phi}{\partial t} = \left(g(I)div\left(\frac{\nabla\phi}{|\nabla\phi|}\right) - \left\langle \nabla g(I), \frac{\nabla\phi}{|\nabla\phi|}\right\rangle\right)|\nabla\phi|. \tag{37}$$

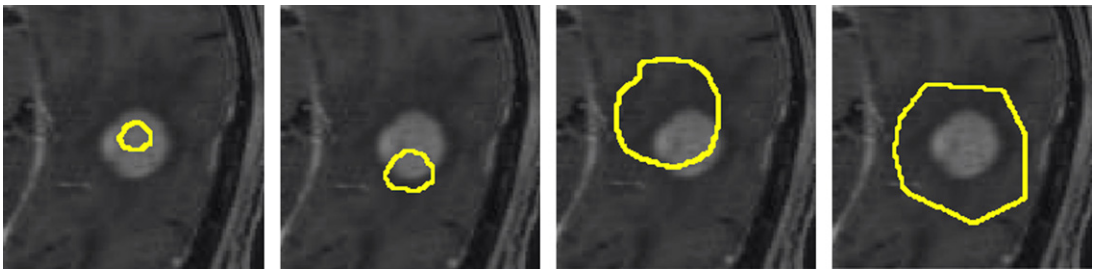

Fig. 2. Various initializations for applying the level set method to the reference slices.

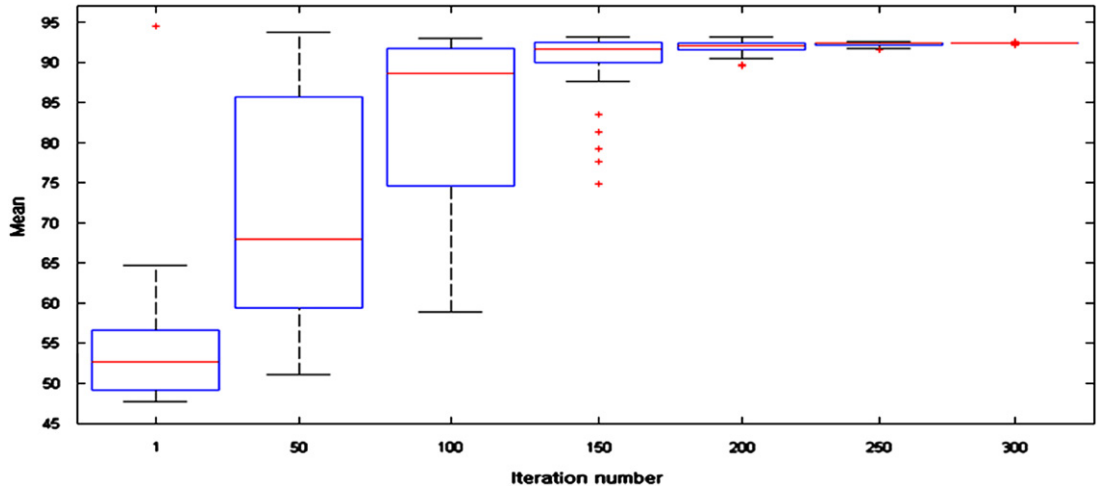

Fig. 3. Box-plot of pixel value means for various initializations.

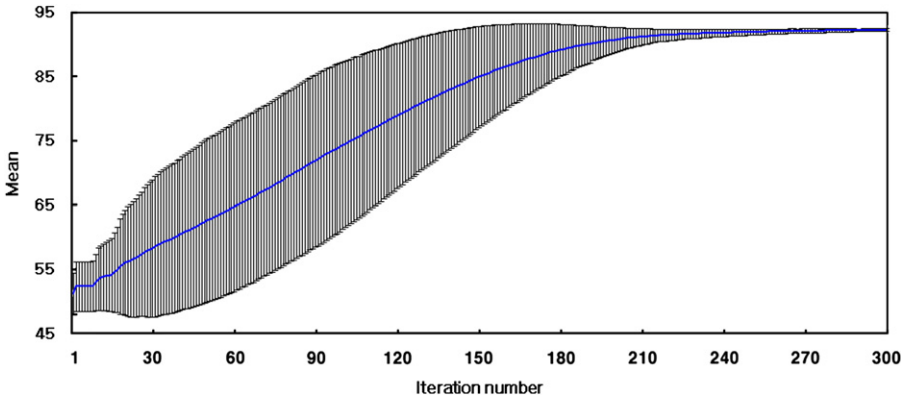

Fig. 4. Confidence intervals for pixel value means for various iteration numbers.

3.4. Hybrid speed function for level set method

In general, active surface models have been developed as paradigms for boundary and region-based methods [17–20]. In this case, we have considered a novel segmentation method using level set evolution by introducing a new speed term. This is defined as the weighted sum of three kinds of measures, terms called robust alignment, active region, and smoothing, which are derived from the respective geometric functionals. This is given as follows:

$$F = \alpha(sign(\langle \mathbf{V}_{GVF}, \nabla\phi \rangle) div(\mathbf{V}_{GVF})) + \beta(\log p_1(I(w)) - \log p_2(I(w))) + \gamma\left(g(I) div\left(\frac{\nabla\phi}{|\nabla\phi|}\right) - \left\langle \nabla g, \frac{\nabla\phi}{|\nabla\phi|} \right\rangle\right). \quad (38)$$

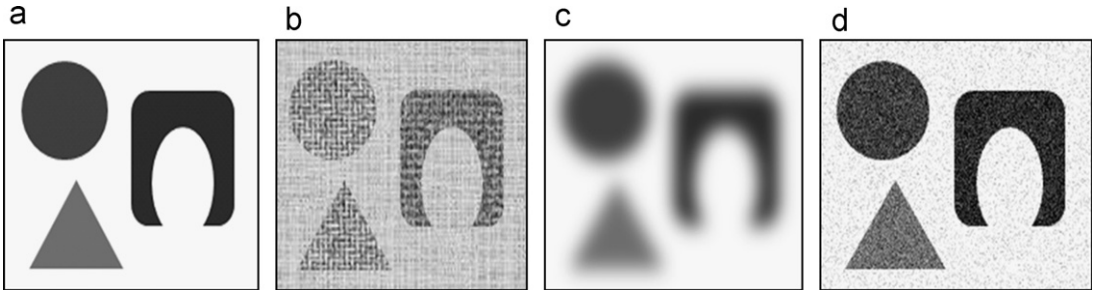

Fig. 5. Various types of synthetic images: (a) original image, (b) texture image, (c) blurring image, and (d) noisy image.

Table 1
PCP, PCN, and ACC measures for segmentation using α,β, and γ for texture image.

(a) PCP

α / β	0.1	0.2	0.3	0.4	0.5	0.6	0.7	0.8
0.1				94.82	96.05	96.82	97.10	97.21
0.2			96.30	96.12	95.93	96.00	96.13	
0.3		96.98	96.95	96.76	96.75	96.28		
0.4	97.00	97.02	97.07	96.78	96.58			γ = 0.1
0.5	96.95	97.13	96.91	96.72				γ = 0.2
0.6	97.17	96.94	96.82					γ = 0.3
0.7	96.95	96.83						γ = 0.4
0.8	96.87							γ = 0.5

(b) PCN

α / β	0.1	0.2	0.3	0.4	0.5	0.6	0.7	0.8
0.1				82.40	78.67	76.57	74.55	71.81
0.2			99.66	99.67	99.65	99.59	97.94	
0.3		99.55	99.39	99.24	98.95	98.27		
0.4	99.51	99.31	98.98	98.36	97.73			γ = 0.1
0.5	99.29	98.89	98.30	97.31				γ = 0.2
0.6	98.86	98.25	97.32					γ = 0.3
0.7	98.22	97.31						γ = 0.4
0.8	97.30							γ = 0.5

(c) ACC

α / β	0.1	0.2	0.3	0.4	0.5	0.6	0.7	0.8
0.1				0.97942	0.97911	0.97997	0.97997	0.97542
0.2			0.98629	0.98595	0.9853	0.98516	0.97962	
0.3		0.98762	0.98643	0.98537	0.9828	0.97627		
0.4	0.98752	0.98619	0.98417	0.97935	0.97101			γ = 0.1
0.5	0.98602	0.98397	0.97836	0.96786				γ = 0.2
0.6	0.98393	0.97757	0.96807					γ = 0.3
0.7	0.9775	0.96807						γ = 0.4
0.8	0.96793							γ = 0.5

So, the corresponding level set formulation of our surface evolution is given by:

$$\phi^{(t)} = \phi^{(t-1)} + \Delta t \cdot F \cdot |\nabla \phi^{(t-1)}|. \quad (39)$$

Finally, in order to ensure that the solution of the partial differential equation is both consistent and stable, it should be guaranteed that the small approximation error does not get amplified as the solution is stepped forward in time. That is, the stability of the solution can be preserved by using the Courant–Friedrichs–Lewy (CFL) condition [21], which asserts that numerical curves or surfaces should move at most in one grid cell at each time step. This results in the CFL time step restriction given by:

$$\Delta t \leq \frac{1}{\max(F, |\nabla \phi|)}. \quad (40)$$

4. Analysis

4.1. Level set initialization

First, in order to show that the proposed method does not depend on the initial values, we have implemented image segmentation using various initial values for up to 300 iterations of the level set function. Fig. 2 shows examples of initial contours obtained from the reference slices.

In Fig. 3, we show box-and-whisker plots of the pixel value means in the segmented region obtained using various iteration numbers for each initialization. This is a demonstration of the robustness of our algorithm to initialization, after applying a suitable number of iterations. Based on this plot, we note that the mean values stabilize and almost converge towards the target value.

Next, Fig. 4 shows the confidence intervals for the pixel value means in the brain MR image obtained using iteration numbers

Table 2
PCP, PCN, and ACC measures for segmentation using α, β, and γ for blurring image.

(a) PCP

	0.1	0.2	0.3	0.4	0.5	0.6	0.7	0.8
0.1				89.93	89.26	89.51	89.09	87.79
0.2			93.77	92.95	92.97	95.28	95.83	
0.3		96.25	95.97	96.23	95.90	95.76		
0.4	96.36	96.31	96.23	95.74	96.42			
0.5	96.38	96.35	96.32	96.24				
0.6	96.41	96.41	96.41					
0.7	96.47	96.45						
0.8	96.54							

(b) PCN

	0.1	0.2	0.3	0.4	0.5	0.6	0.7	0.8
0.1				89.08	85.47	84.07	80.19	79.61
0.2			95.27	93.02	92.80	89.02	88.87	
0.3		97.44	96.76	93.84	91.88	90.42		
0.4	97.71	97.50	97.32	97.01	94.06			
0.5	97.71	97.63	97.43	97.20				
0.6	97.71	97.66	97.47					
0.7	97.71	97.67						
0.8	97.72							

(c) ACC

α / β	0.1	0.2	0.3	0.4	0.5	0.6	0.7	0.8
0.1				0.83226	0.88987	0.86876	0.95331	0.96455
0.2			0.92706	0.96016	0.95993	0.95944	0.95479	
0.3		0.88528	0.88319	0.93072	0.94358	0.94431		
0.4	0.88005	0.86887	0.86005	0.84881	0.92869			γ = 0.1
0.5	0.87006	0.8651	0.85685	0.81002				γ = 0.2
0.6	0.85932	0.85241	0.80938					γ = 0.3
0.7	0.84422	0.80621						γ = 0.4
0.8	0.80839							γ = 0.5

1–300. It can be seen that as the iteration number increases, the mean values stabilize and also the length of the confidence interval rapidly decreases.

4.2. Study of the properties of three parameter values

In this analysis, we describe the properties of three parameters in the hybrid speed function that should be set by the user. These parameters are the following terms: robust alignment (α), active region (β), and smoothing (γ), and they need to be weighted properly in order to guide the evolving surface under different image conditions. Therefore, to assess the segmentation performance obtained by adjusting the parameter values of α, β, and γ, we apply our level set procedure to the synthetic original, texture, blurring, and noisy images shown, respectively, in Fig. 5.

In this case, we have used the measure proposed by Fukunaga [22] and Kornel et. al [23], in order to numerically evaluate the segmentation results obtained using various values of the three parameters. This measure is defined using False Positive (FP), False Negative (FN), True Positive (TP), and True Negative (TN). Classifying object data as a background is considered a FP and classifying background data as an object is considered a FN. TP and TN are the cases where an object is classified as an object and a background is classified as a background, respectively. The accuracy of the segmentation result can be estimated using the following three equations.

First, Chou and Fasman [24,25] used the percentage of correctly predicted (PCP) objects

$$PCP = 100\frac{TP}{TP+FN}. \tag{41}$$

It is the same as the sensitivity expressed as a percentage. But, this number alone provides no information whatever about false positives.

Second, we have considered another measure of false positives. It can be defined by the percentage of correctly predicted

Table 3
PCP, PCN, and ACC measures for segmentation using α, β, and γ for noisy image.

(a) PCP

β \ α	0.1	0.2	0.3	0.4	0.5	0.6	0.7	0.8
0.1				96.53	96.69	96.84	97.29	97.81
0.2			98.33	98.12	98.10	97.96	98.04	
0.3		98.78	98.72	98.68	98.73	98.77		
0.4	98.88	99.09	99.23	99.10	99.00			γ = 0.1
0.5	99.17	99.25	99.24	99.17				γ = 0.2
0.6	99.30	99.31	99.25					γ = 0.3
0.7	99.33	99.28						γ = 0.4
0.8	99.29							γ = 0.5

(b) PCN

β \ α	0.1	0.2	0.3	0.4	0.5	0.6	0.7	0.8
0.1				82.54	80.58	80.09	78.42	74.08
0.2			99.83	99.81	99.82	99.71	97.68	
0.3		99.73	99.62	99.37	98.14	96.70		
0.4	99.68	99.45	98.41	97.11	96.34			γ = 0.1
0.5	99.36	98.12	96.92	96.14				γ = 0.2
0.6	97.93	96.84	96.03					γ = 0.3
0.7	96.77	95.90						γ = 0.4
0.8	95.84							γ = 0.5

(c) ACC

β \ α	0.1	0.2	0.3	0.4	0.5	0.6	0.7	0.8
0.1				0.98958	0.99025	0.99035	0.99082	0.98941
0.2			0.99573	0.99519	0.99462	0.99426	0.99299	
0.3		0.99659	0.99653	0.99629	0.99566	0.99402		
0.4	0.99723	0.99699	0.99673	0.99506	0.99269			γ = 0.1
0.5	0.99743	0.99706	0.99482	0.99279				γ = 0.2
0.6	0.99733	0.99532	0.99302					γ = 0.3
0.7	0.99573	0.99329						γ = 0.4
0.8	0.99312							γ = 0.5

non-object (PCN)

$$PCN = 100\frac{TN}{TN+FP}. \quad (42)$$

Third, the overall accuracy (ACC) of the segmentation result can be estimated using the following equation;

$$ACC = \frac{TP+TN}{TP+TN+FP+FN}. \quad (43)$$

Tables 1–3 show the comparison of segmentation performance for possible values of the three parameters α,β, and γ in the three synthetic images, i.e., texture, blurred, and noisy image. Table 1 presents the case that the robust alignment term is tuned to play the dominant role in the segmentation of the texture image. On the other hand, the active region term makes little contribution to exact segmentation. In other words, the alignment term in the speed function has a greater influence than the other terms on segmentation of the texture image.

Table 2 shows that the active region term makes the dominant contribution to the blurred image, but neither the robust alignment term nor the smoothing term contribute to good segmentation.

For noisy images, Table 3 shows that the smoothing term is the important factor while the robust alignment term and the active region term both make little contribution to good segmentation.

Fig. 6 shows the optimal segmentation results obtained using the proposed parameters in the texture, blurring and noisy images, respectively.

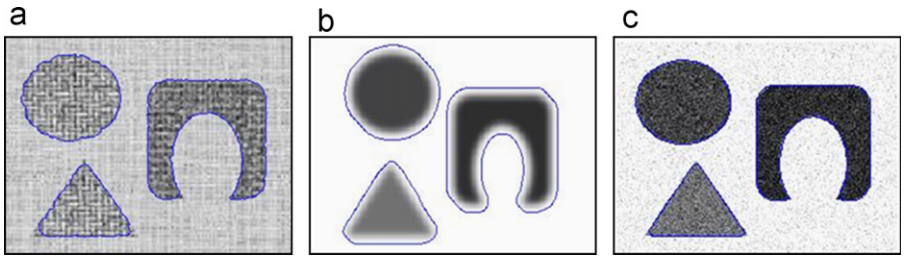

Fig. 6. Results of segmentation using α, β and γ parameter values of the proposed speed function: (a) α=0.5, β=0.2, γ=0.3, (b) α=0.1, β=0.6, γ=0.3, (c) α=0.2, β=0.3, γ=0.5.

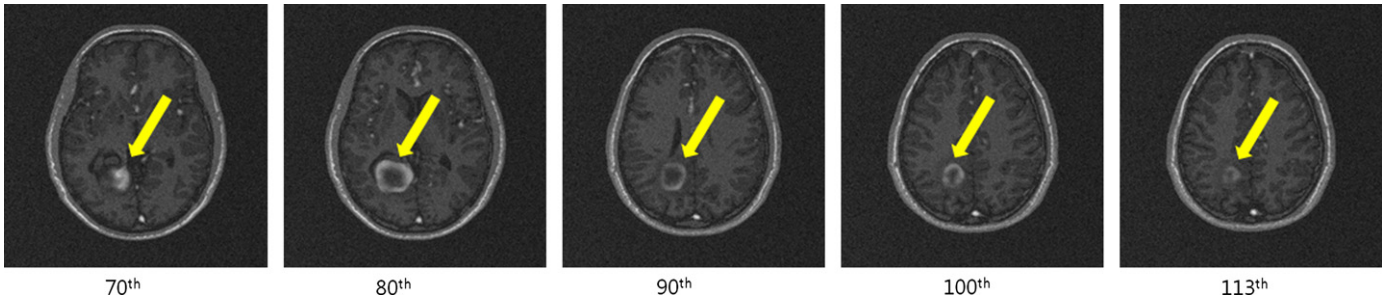

Fig. 7. Example slices of original brain MR tumor images.

Table 4
Quantitative comparison of four segmentation methods.

Volume	Volume (mm^3)					Overlap (JM %)				Hausdorff (mm)			
	MS	HB	MA	MV	EB	HB	MA	MV	EB	HB	MA	MV	EB
Head 1	2560	2438	2394	2399	3700	93.95	92.54	92.73	38.32	1.2654	1.3361	1.3361	4.3591
Head 2	3977	3848	3862	3871	3495	94.17	94.47	94.72	42.44	1.6956	1.6250	1.6250	3.8010
Head 3	4494	3430	3166	3563	661	72.52	67.67	73.30	9.41	3.1527	3.4463	3.4616	6.5389
Head 4	28074	26462	25277	23992	3685	89.76	86.55	84.04	7.78	2.6910	2.7693	2.6693	4.1183
Lung	9710	9016	9099	6160	74	92.34	93.36	63.44	0.76	2.4094	2.4238	2.8049	5.0563

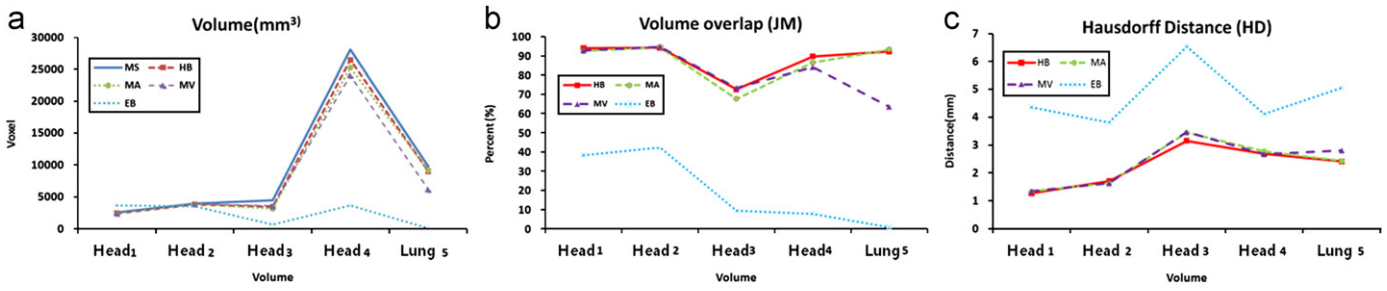

Fig. 8. Quantitative comparison of the results of the HB, MA and MV schemes using two metrics. (a) Volume with manual segmentation, (b) volume overlap (JM), and (c) Hausdorff distance (HD).

5. Experimental results

We compare the performance of our hybrid speed function with traditional speeds, such as mean speed (Chan & Vese [7]), mean-variance speed (Rousson & Deriche [26]), and edge based speed (Caselles et al. [16]), and validate the segmentation results. Five datasets of various patients acquired from the UNC CASILab [28] are used to evaluate the segmentation performance for each method. These include four brain MR volume datasets with a tumor and one lung CT volume dataset. Each MR and CT volume images has an in-plane resolution of $256 \times 256 \times 120$ and $512 \times 512 \times 330$ a voxel size of $1 \times 1 \times 1$ mm, respectively. In this case, we focused on MR images of a brain tumor where the ROI is indicated by an arrow, as shown in Fig. 7.

The results of 3D segmentation in terms of the mean speed, mean-variance speed, edge-based speed and our hybrid speed for MR volume images with tumor are compared with manual segmentation. Here, the manual segmentation has been provided

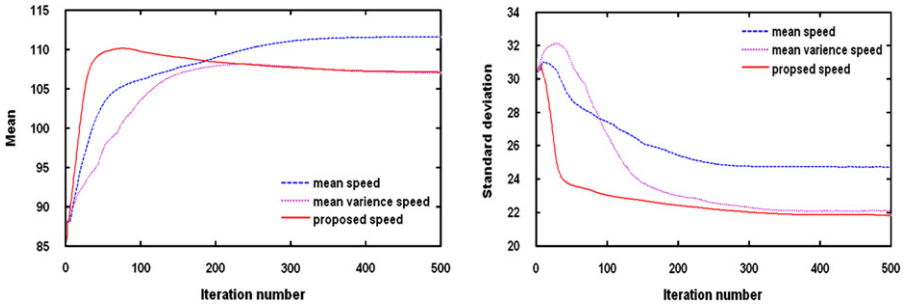

Fig. 9. A comparison of the convergence rate of our method with MA, MV methods.

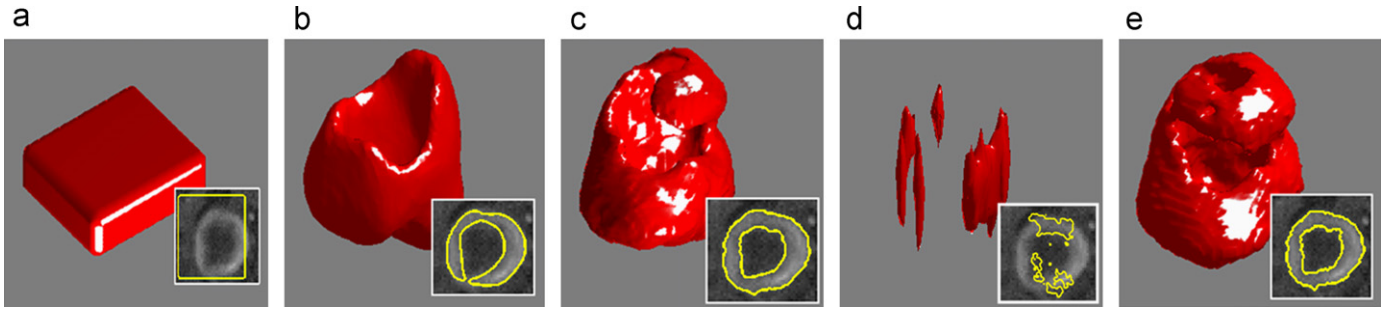

Fig. 10. A comparison of segmentation results for medical volume images. (a) Initial surface, (b) mean speed, (c) mean-variance speed, (d) edge-based speed, and (e) hybrid speed.

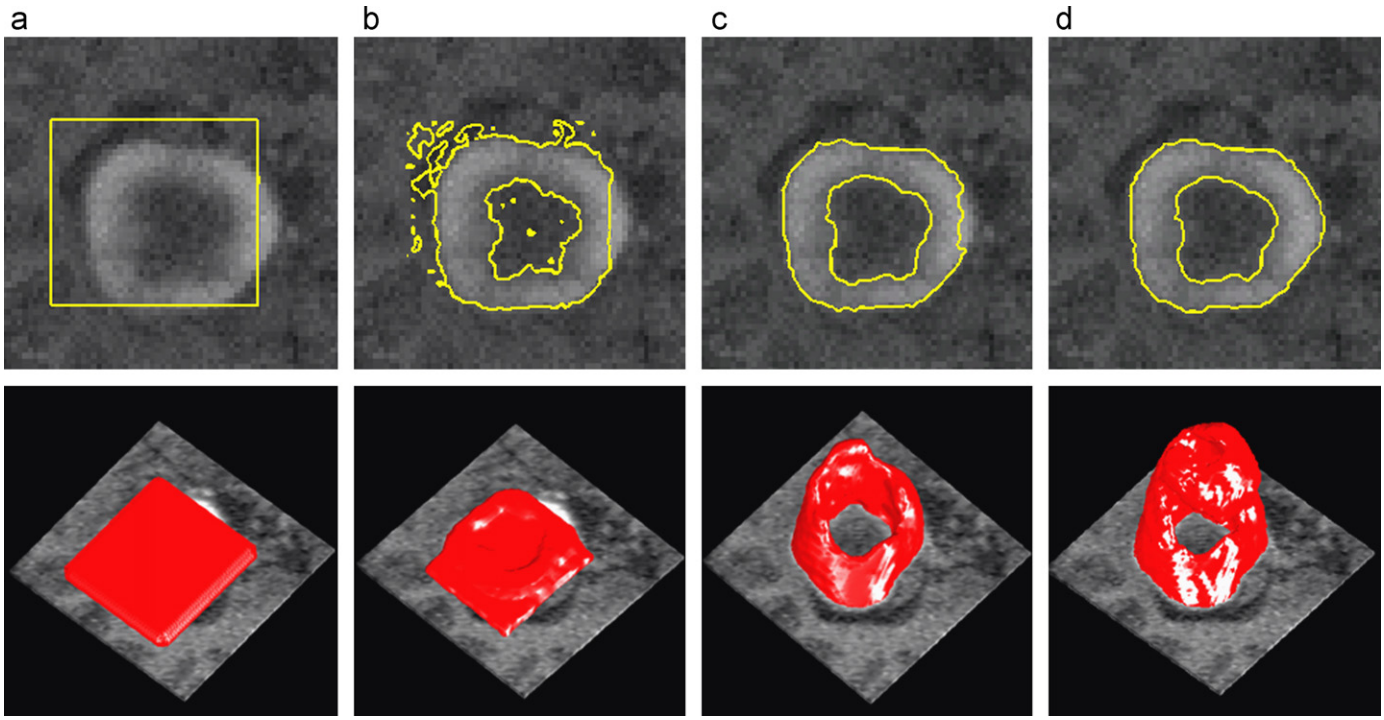

Fig. 11. Tumor segmentation results of the proposed segmentation scheme. (a) Initial surface, (b) intermediate-closer to initial, (c) intermediate-closer to final, and (d) final segmentation result.

with the data sets obtained from the authors' team performing the segmentation. In this paper, two validation metrics are used. One is Jaccard's Measure (JM) or the volume overlap metric. This is the normalized voxel intersection count for the pair of segmentations Ω_M and Ω_T, where Ω_M and Ω_T denote the set of tumor voxels in manual segmentation and the corresponding segmentation resulting from each speed function, respectively. This is defined by:

$$JM = \frac{\#(\Omega_M \cap \Omega_T)}{\#(\Omega_M \cup \Omega_T)}. \quad (44)$$

The other is the Hausdorff Distance (HD) which defines the maximum surface distance. This measure is extremely sensitive to outliers and may not reflect the overall degree of matching.

$$Hausdorff = \max(D_1(A,B), D_1(B,A)) \quad (45)$$

where A and B are the reference and result surface of the algorithm respectively, and $D_1(A,B) = \max_{x \in A}(\min_{x \in B}(\|x-y\|))$.

The quantitative validation of the four segmentation methods with the Hybrid Speed (HB), Mean Speed (MA), Mean-Variance Speed (MV), and Edge-based Speed (EB) are presented in Table 4.

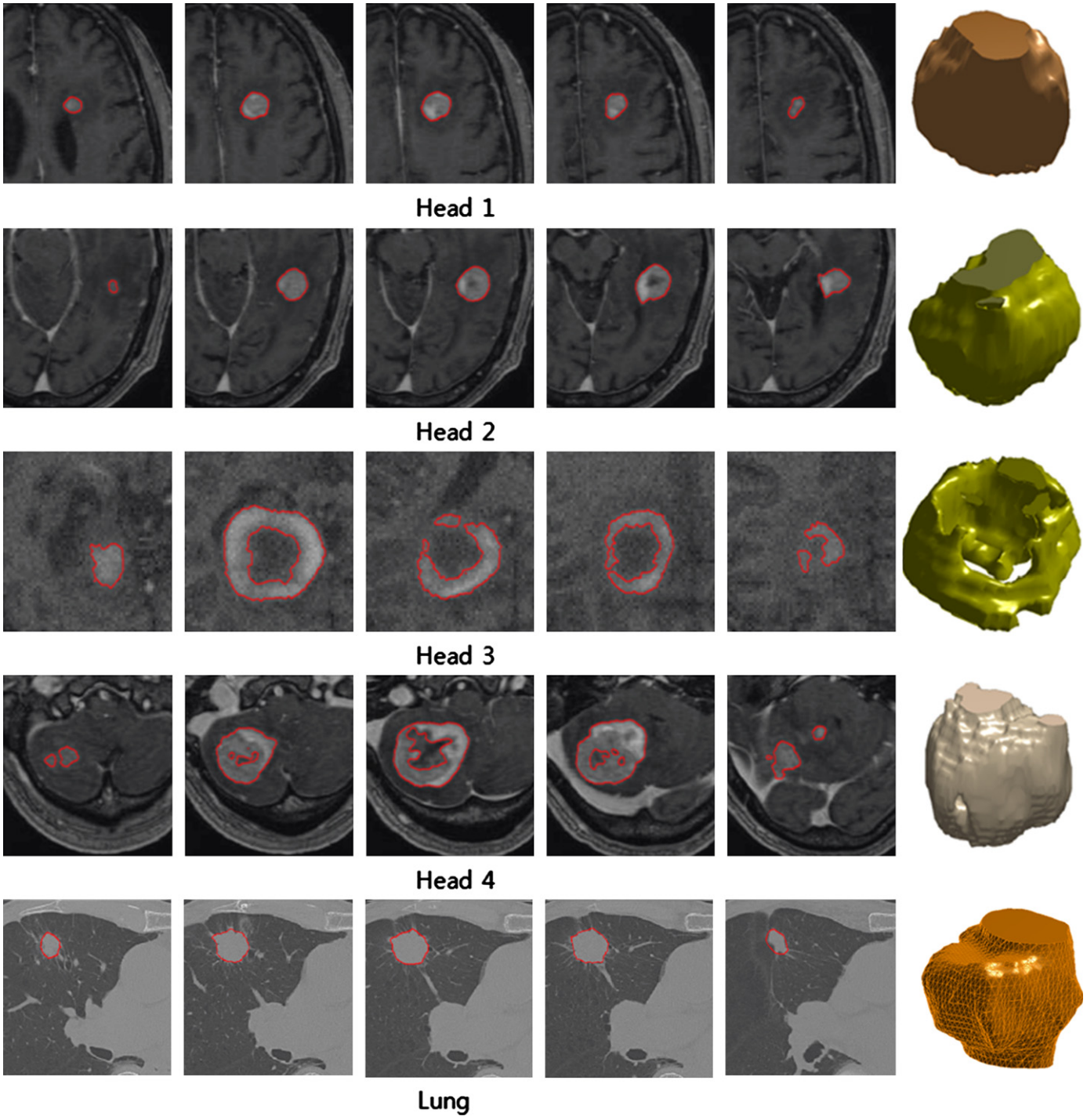

Fig. 12. Cross-sections of extracted tumor surfaces in addition to the 3D view of corresponding surfaces.

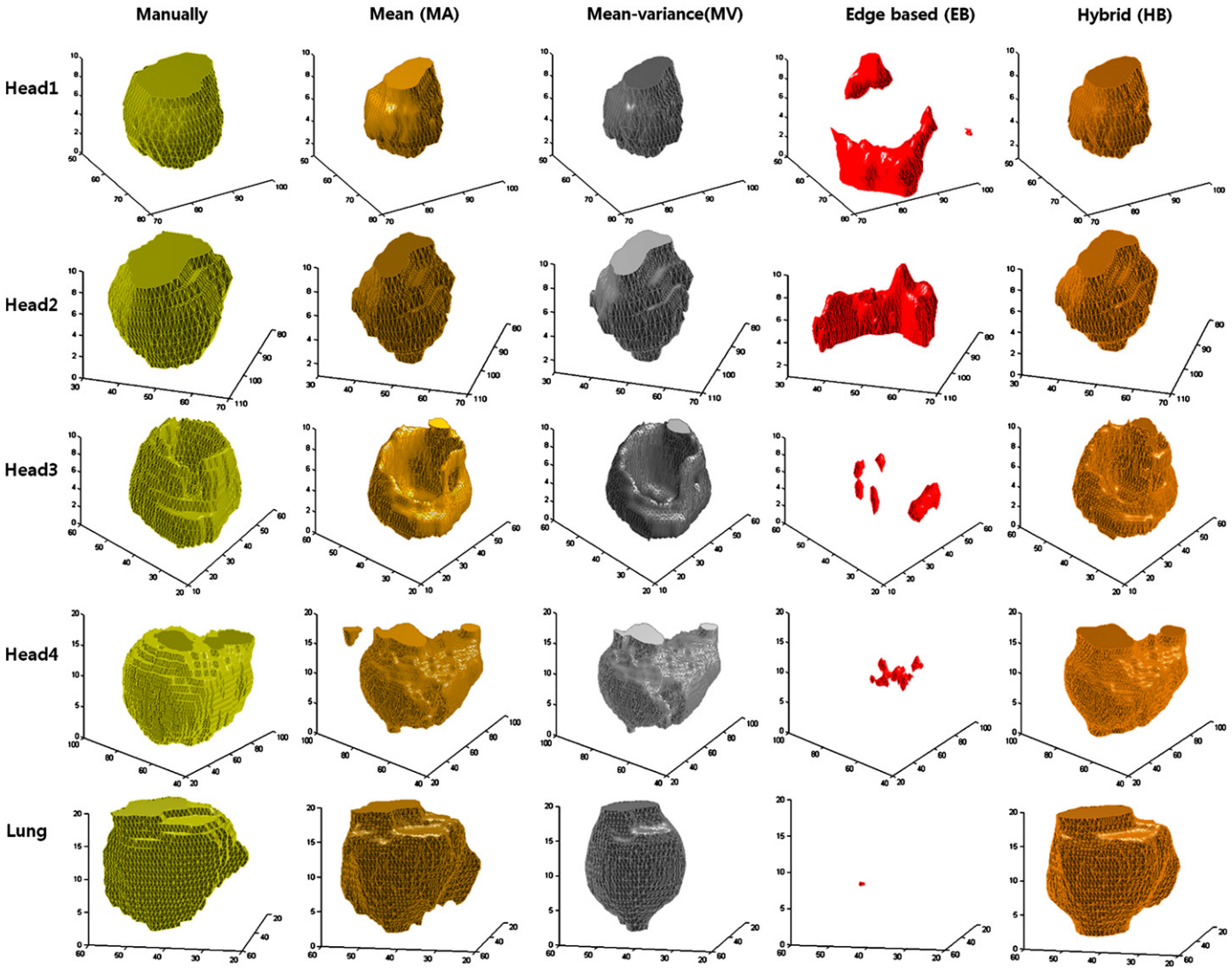

Fig. 13. A comparison of segmentation results for medical volume images.

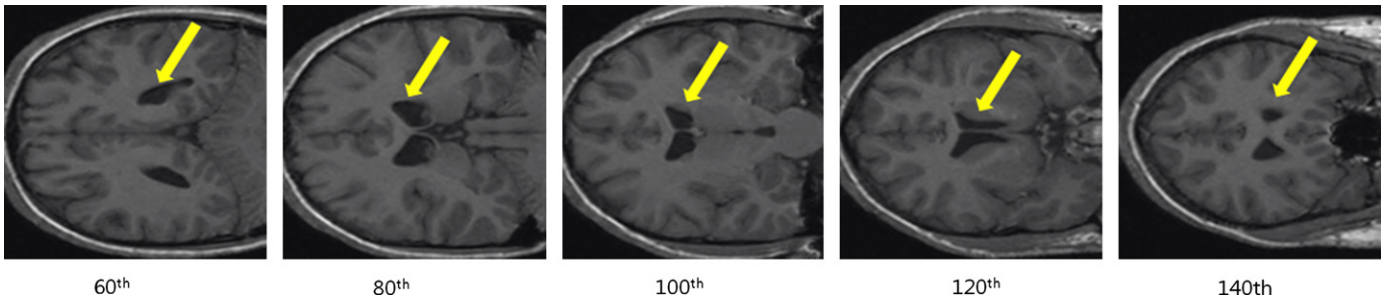

Fig. 14. Example slices of brain MR images for CerebroSpinal Fluid (CSF).

First, in the first column of Table 4, we note that the volume size of our segmentation method with respect to manual segmentation is 91.09% overall. On the other hand, the values for the other three methods are 88.96% (MA), 83.85% (MV), and 52.20% (EB), respectively. Hence, the volume size of our segmentation method approximates that of manual segmentation better than the other methods.

Second, in the second column of Table 4, JM in the HB scheme varies from 72.52% to 94.17%, in the MA scheme it varies from 67.67% to 94.47%, and in the MV scheme it varies from 63.44% to 94.72%. However, the EB scheme obtained lower values than the other three schemes (it varies from 0.76% to 42.44%). The JM values show that the amount of volume overlap of our method for various medical datasets is higher than the other methods, thus demonstrating that our method is more robust and reliable with respect to the size and complexity of tumors or normal tissue. Thus, the HB scheme generally performs better than the other schemes.

Third, in the third column of Table 4, the HB scheme varies from 1.2654 mm to 3.1527 mm, in the MA scheme it varies from 1.3361 mm to 3.4463 mm, and in the MV scheme it varies from 1.3361 mm to 3.4616 mm. However, the EB scheme obtained

higher values than other three schemes (it varies from 3.8010 mm to 6.5389 mm). In this case a low HD value is indeed an indicator of good matching between two surfaces, and a high HD value does not imply poor matching. Because two surfaces that are fairly matched may still have a large HD value due to some outliers in the matching distances between them. However, the results for the HD metric indicate that our segmentation method is very reliable.

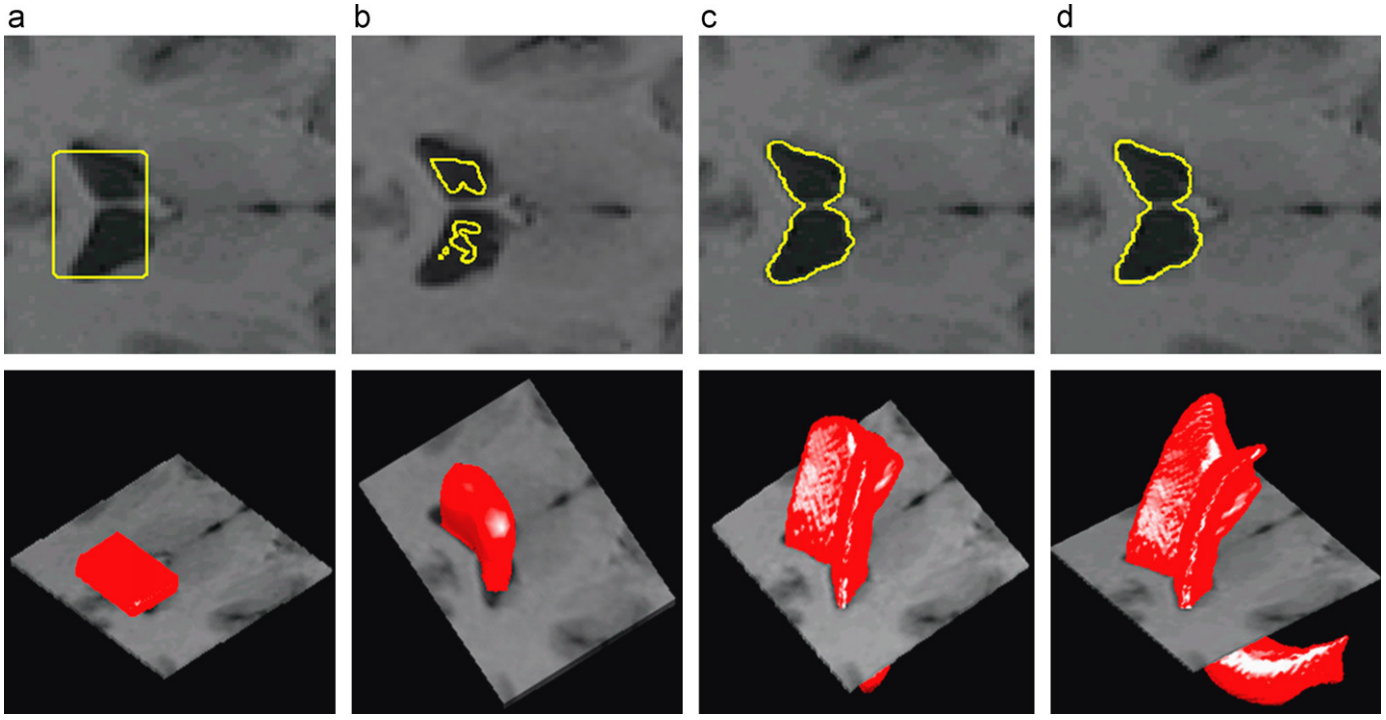

Fig. 15. CSF segmentation results of the proposed segmentation scheme. (a) Initial surface, (b) intermediate-closer to initial, (c) intermediate-closer to final, and (d) final segmentation result.

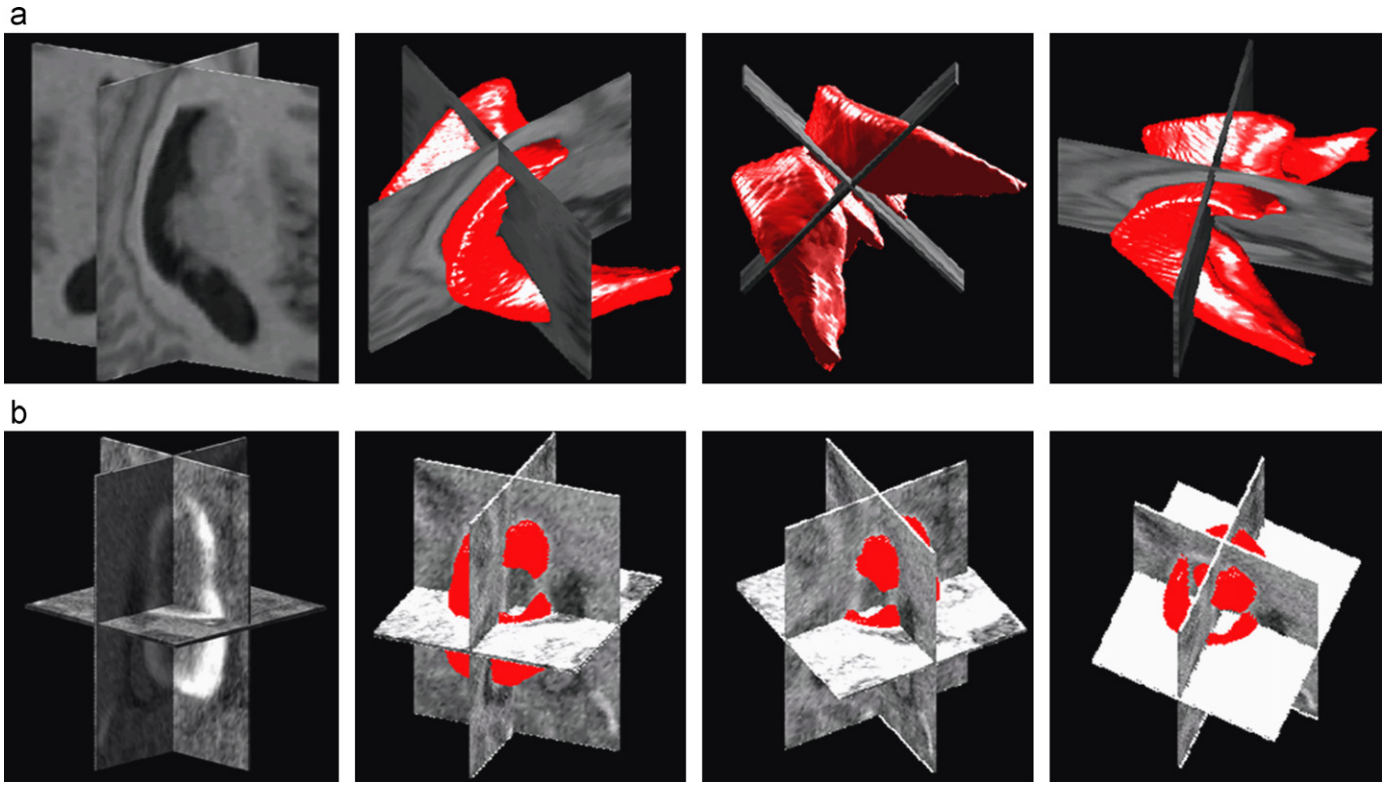

Fig. 16. Visualization of segmentation results for various views. (a) CSF region in brain MR image and (b) tumor region in abnormal brain MR image.

Fig. 8 shows the graphical diagram for the quantitative comparison of the HB, MA, MV, and EB schemes. As seen in Fig. 8(b), the JM score is generally higher than the other ones. The proposed HB scheme gives the highest JM values except for Head 2, where MV performs the best. Furthermore, the HD scheme works better for simple and convex/concave tumors than for complex ones. This can also be verified in Fig. 8(c). However, the HB scheme performs better than the other two schemes except for Head 3, which is the complex tumor. This is the reason for the third regularization term.

The speed or convergence rate of the three algorithms (HB, MA, MV) can be compared using the number of iterations needed for exact segmentation. Utilizing a speed comparison is a valid approach, since the time taken to complete iteration in the three algorithms is nearly the same. In Fig. 9, the mean and standard deviation of the intensity values in the segmented tissue are displayed according to the iteration numbers for the three algorithms. Based on these results, we note that the convergence rate of our method is faster and more stable than the other methods.

Next, the 3D segmentation result obtained using the proposed approach for the volume datasets is compared with the segmentation results obtained using the other methods. Fig. 10(a)–(e) shows the initial surface and the segmented volume surfaces given by the Mean Speed (MA), Mean-Variance Speed (MV), Edge-based Speed (EB), and the Hybrid Speed (HB), respectively. The experimental results showed that the proposed segmentation method was more accurate than the other methods.

We also applied the proposed segmentation method to the brain MR volume dataset with tumor. In each case, the first row shows one slice and the second row shows the 3D volume. The initial surface was located by a small cube inside the object, as shown in Fig. 11(a) and from Fig. 11(b) and (c), we can observe that the initial surface splits and evolves towards the boundaries of the tumor. Also, our method segments the brain MR image accurately for the tumor boundaries, as shown in Fig. 11(d).

Fig. 12 shows the cross-sections of extracted tumor surfaces using the hybrid speed function with some of their image slices in addition to the 3D view of the corresponding surfaces for the five datasets used in the above experiment.

Fig. 13 shows the comparison of segmentation results for five medical volume images with four different methods. Based on Fig. 13, the Mean Speed (MA) and Mean-Variance Speed (MV) methods can achieve acceptable results with manual segmentation. However, the Edge-based Speed (EB) method cannot be expanded any more towards the object. But, our proposed method, which is the Hybrid Speed (HB) method, obtains more similar results to manual segmentation than the MA and MV methods.

Next, we have also applied our segmentation method to the normal tissue of brain MR images where the ROI is indicated by an arrow in Fig. 14. Each MR volume image has an in-plane resolution of $166 \times 131 \times 200$ and a voxel size of $1 \times 1 \times 1$ mm.

Fig. 15 shows the final segmentation results of CSF obtained by applying the proposed approach to the brain MR volume dataset. In each case, the first row shows one slice image and the second row shows the 3D volume images. The initial level set is a hexahedron surface for which the initial rectangle is placed around the ROI in the reference slice in Fig. 15(a), and the intermediate results are shown in Fig. 15(b) and (c), respectively. The hybrid method accurately segments the anatomical region of the brain MR image, as shown in Fig. 15(d).

To visualize the segmentation results of the brain MR images, we conducted an experiment on the 3D volume dataset. Fig. 16(a) and (b) show the 3D rendering results of the segmented CSF region in the brain MR images and the tumor region in the abnormal brain MR images obtained using the proposed level set method with respect to its rotated view.

6. Conclusions

We have presented a detection method for anatomic structures in volume medical images using the level set method with a new hybrid speed function. The level set procedure can segment the volume images much more accurately, and it has less sensitively to noise. It works by exploiting three speed terms, which are robust alignment, active region, and smoothing. We analyzed the characteristics of these terms using the original, texture, blurring, and noisy images. The experimental results show that our method clearly outperforms the approaches it was compared against, but it still varies from the ground truth volume images.

References

[1] S. Lakare, 3D segmentation techniques for medical volumes, Res. Rep. (2000).
[2] X. Han, C. Xu, J.L. Prince, A topology preserving level set method for geometric deformable models, IEEE Trans. PAMI 25 (6) (2003) 755–768.
[3] J.A. Sethian, Level Set Methods and Fast Marching Methods: Evolving Interfaces in Geometry, Fluid Mechanics, Computer Vision, and Materials Science, Cambridge University Press, 1999.
[4] M. Droske, B. Meyer, M. Rumpf, C. Schaller, An adaptive level set method for medical image segmentation, Proceedings of the Annual Symposium on Information Processing in Medical Imaging, 2001.
[5] A. Lefohn, J. Cates, R. Whitaker, Interactive GPU-based level sets for 3D brain tumor segmentation, Technical Report, University of Utah, School of Computing Tech, April 2003.
[6] M. Leventon, W. Grimson, O. Faugeras, Statistical shape influence in geodesic active contours, IEEE Conference computer Vision and Pattern Recognition, vol. 1, pp. 316–323, 2000.
[7] T.F. Chan, L.A. Vese, Active contours without edges, IEEE Trans. Image Process. 10 (2) (2001) 266–277.
[8] Z. Zhou, J. You, P. Heng, D. Xia, Cardiac MR image segmentation and left ventricle surface reconstruction based on level set method, Studies Health Technol. Inf. (2005) 629–632.
[9] Q. Su, K.-Y.K. Wong, G.S.K. Fung, A semi-automatic clustering-based level set method for segmentation of endocardium from MSCT images, Annual International Conference of the IEEE Engineering in Medicine and Biology Society, Lyon, France, pp. 6023–6026, 2007.
[10] H. Khotanlou, J. Atif, O. Colliot, I. Bloch, 3D brain tumor segmentation using fuzzy classification and deformable models, Workshop on Fuzzy Logic and Appl. (2005) 312–318.
[11] S. Ho, H. Cody, G. Gerig, Snap: a software package for user-guided geodesic snake segmentation, Technical report, University of North Carolina, Chapel Hill, 2003.
[12] R. Kimmel, Fast edge integration, Geometric Level Set Methods in Imaging, Vision, and Graphics, Springer, 2006, pp. 59-79.
[13] R. Goldenberg, R. Kimmel, E. Rivlin, M. Rudzsky, Cortex segmentation: a fast variational geometric approach, IEEE Trans. Med. Imaging 21 (2) (2002) 1544–1551.
[14] C. Xu, J.L. Prince, Snakes, shapes, and gradient vector flow, IEEE Transa. Image Process. 7 (3) (1998) 359–369.
[15] D. Jayadevappa, S. Srinivas Kumar, D.S. Murty, A new deformable model based on level sets for medical image segmentation, IAENG Int. J. Comput. Sci. 36 (3) (2009).
[16] V. Caselles, R. Kimmel, G. Sapiro, Geodesic active contours, Int. J. Comput. Vision 22 (1) (1997) 61–79.
[17] Y. Zhang, B.J. Matuszewski, L.K. Shark, C.J. More, Medical image segmentation using new hybrid level set method, International Conference Biomedical Visualization, 2008.
[18] O. Michailovich, Y. Rathi, A. Tannenbaum, Image segmentation using active contours driven by the Bhattacharyya gradient flow, IEEE Trans. Image Process. 16 (11) (2007) 2787–2801.
[19] S. Dambreville, A. Tannenbaum, A. Yezzi, M. Niethammer, A variational framework combining level-set and thresholding, British Machine Vision Conference, 2007.
[20] S. Taheri, S.H. Ong, V.F.H. Chong, Level-set segmentation of brain tumors using a threshold-based speed function, Image and Vision Computing 28 (2010) 26–37.
[21] S. Osher, N. Paragios, Geometric Level Set Methods in Imaging, Vision, and Graphics, Springer-Verlag, New York Berlin Heidelberg, 2003.
[22] K. Fukunaga, Introduction to Statistical Pattern Recognition, second edn., Academic Press, SanDiegoCA, USA, 1990 ISBN: 0-12269851-7 〈http://www.academicpress.com〉.
[23] P. Kornel, M. Bela, S. Rainer, D. Zalan, tg. Xsolt, F. Janos, Application of neural network in medicine, Diag. Med. Technol. 4 (3) (1998) 538–546.
[24] P.Y. Chou, G.D. Fasman, Empirical predictions of protein conformations, Ann. Rev. Biochem. 47 (1978) 251–276.
[25] P.Y. Chou, G.D. Fasman, Prediction of the secondary structure of proteins from their amino acid sequence, Adv. Enzymol. Relat. Areas Mol. Biol. 47 (1978) 45–148.

[26] M. Rousson, and R. Deriche, A variational framework for active and adaptive segmentation of vector valued images, IEEE Workshop on Motion and Video Computing, 2002.
[27] X.-F. Wang, D.-S. Huang, H. Xu, An efficient local Chan-Vese model for image segmentation, Pattern Recognition 43 (2010) 603–618.
[28] UNC Computer-Assisted Surgery and Imaging Laboratory, 〈http://casilab.med.unc.edu〉.

Myungeun Lee received the B.S., M.S. and Ph.D. degrees in Electronics Engineering from Mokpo National University, Korea, in 1998, 2001 and 2007, respectively. From 2007 to 2011, she was a postdoctoral research fellow and a research professor in the Department of Computer Science, Chonnam National University, Korea. Since 2011, she has been a senior member of research staff in Medical Research Center, Seoul National University, Korea. Her research interests are medical image processing, pattern recognition, and 3D image reconstruction.

Wanhyun Cho received both B.S. degree and M.S. degree from the Department of Mathematics, Chonnam National University, Korea, in 1977, 1981, respectively and Ph.D. degree from the Department of Statistics, Korea University, Korea in 1988. He is now teaching in Chonnam National University. His research interests are statistical modeling, pattern recognition, image processing, and medical image processing.

Sunworl Kim received the B.S. degree in Information Statistics from Korea National Open University, Korea, in 2004, and the M.S. degrees in Statistics from Chonnam National University in 2006. She is currently studying the Ph.D. course in the Department of Statistics, Chonnam National University, Korea. Her research interests include medical image segmentation, registration, pattern recognition and statistical modeling.

Soonyoung Park received B.S. degree in Electronics Engineering from Yonsei University, Seoul, Korea in 1982 and M.S. and Ph.D. degrees in Electrical and Computer Engineering from State University of New York at Buffalo, in 1986 and 1989, respectively. From 1989 to 1990, he was a Postdoctoral Research Fellow in the department of Electrical and Computer Engineering at the State University of New York at Buffalo. Since 1990, he has been a Professor with Department of Electronics Engineering, Mokpo National University, Korea. His research interests include biomedical image processing, image protection and authentication, and image retrieval techniques.

Jong Hyo Kim received the B.Sc., M.Sc, and Ph.D. degrees in Electronics Engineering from Seoul National University, Seoul, Korea in 1982, 1986, and 1994, respectively. He is currently an Associate Professor at Department of Intelligent Convergence Systems, Graduate School of Convergence Science, and Department of Radiology, College of Medicine, Seoul National University. His research interests include computer aided diagnosis, and computational modeling in medical imaging.